REMOTE SENS. ENVIRON. 46:146–163 (1993)

Recurrent Patterns in Surface Thermal Fronts Associated with Cold Filaments along the West Coast of North America

*James T. Randerson** *and James J. Simpson*†

Previous studies indicate that cold filaments off northern California have sharp southern (s-type) and diffuse northern (d-type) thermal boundaries. In this study, 44 AVHRR satellite images taken from three coastal regions in the California Current System (northern, central, and Baja California) over a period of 10 years were used to examine the regional variation in surface frontal structure associated with cold filaments. The images were specifically chosen from months where past mean wind conditions indicated upwelling occurred because cold filaments appear to be more abundant during the upwelling season. The images also were chosen to provide independent realizations of filament structure. Distributions of average gradient magnitude as a function of gradient angle were used to provide a more compact representation of the frontal information contained in each image. An analysis of these distributions shows that the sharp / diffuse boundary structure associated with cold filaments observed in shipboard data dominates the total surface frontal structure found in satellite data for two of the three regions studied. The recurrent, ubiquitous patterns found in the satellite-determined frontal structure are discussed in terms of their potential effects on acoustic propagation and regional implications on ecological community structure in the California Current System.

INTRODUCTION

Filaments can transport cold coastal water to distances as far as several hundred kilometers offshore into the California Current. The filaments are narrow jets that travel on the surface and in the mixed layer at velocities that can exceed 0.5 m s^{-1} (Davis, 1985a,b; Kosro, 1987; Huyer and Kosro, 1987; Strub et al., 1991). Transport associated with the filaments can significantly affect chemical distributions and biological populations, especially when the filaments interact with either offshore (e.g., Simpson, 1984; Haury, 1984) or coastal (e.g., Traganza et al., 1981; Owen, 1989; Hayward and Mantyla, 1990) mesoscale eddies. Mesoscale filament structure has been known to last for weeks and depends on local wind conditions. The fine structure associated with the filaments, however, varies on a time scale of only a few days (Washburn and Armi, 1988).

One of the most striking features of cold filament mechanics is the dissimilarity of the boundaries that separate the cold filament from the warmer water in the surrounding area (e.g., Flament et al., 1985; Kosro and Huyer, 1986; and Ramp et al., 1991). Southern boundaries of filaments, hereinafter called s-type boundaries (for sharp transition), typically have a sharp transition in sea surface temperatures (SST) from cold to hot water. The northern boundaries, hereinafter called d-type boundaries (for diffuse transition), usually exhibit a smoother, more diffuse transition in SST from the warm water north of the filament into the filament's center. Both density compensated (e.g., Flament et al., 1985; Kosro and Huyer, 1986; Rienecker and Mooers, 1989) and non-density compensated (e.g., Kosro and Huyer, 1986; Reinecker et al., 1985; Ramp et al., 1991) s-type boundaries have been observed.

The purpose of this study is to further quantify temperature frontal patterns found in regions of recurrent, cold filaments by using Advanced Very High Resolution Radiometer (AVHRR) imagery taken during the last 10 years off the west coast of North America. These data are used to determine regional differences in the strength and orientation of surface temperature fronts associated with cold filaments in the California Current System. Understanding the nature of recurrent regional

* Stanford University
† Scripps Institution of Oceanography, La Jolla

Address correspondence to James J. Simpson, Scripps Inst. of Oceanography, Scripps Satellite Oceanography Ctr., La Jolla, CA 92093-0237.

Received 26 December 1991; revised 11 December 1992.

0034-4257 / 93 / $6.00

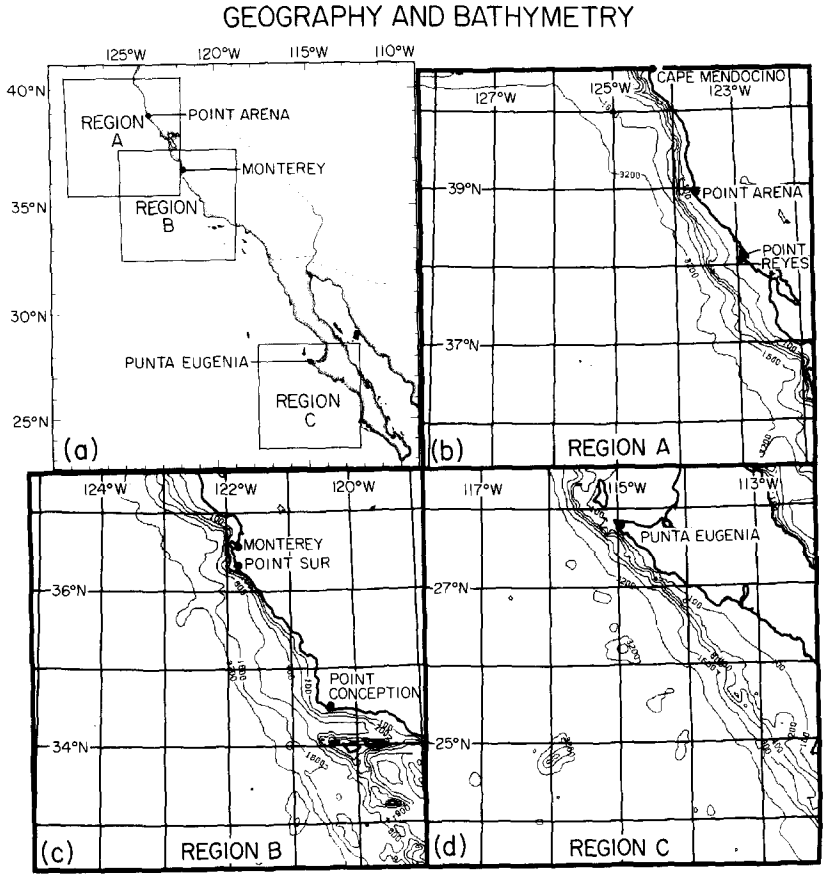

Figure 1. a) Overview of the west coast of North America from Baja California to northern California. Coastlines, bathymetry, and geographical grids are shown for the three study areas: b) Region A (northern California); c) Region B (central California); and d) Region C (Baja California).

patterns in strong near-surface thermal gradients has important implications for at least two areas of oceanic interest: 1) acoustic transmission in the oceanic mixed layer and 2) distributions of pelagic life-forms in the oceans.

DATA

Here, a brief discussion of the AVHRR data and image preprocessing steps used in this study is given.

Data Base Construction

Forty-four AVHRR images centered at three locations off the west coast of North America (Fig. 1a) were used in the present study. Region A off northern California (Fig. 1b) has complex bathymetry and coastline north of Point Arena (i.e., Mendocino Escarpment) and relatively smooth bathymetry and coastline between Point Arena and Point Reyes. The region has relatively strong equatorward winds favorable for coastal upwelling from April through October (Fig. 2). Region B is located off central California (Fig. 1c), and has a more complex bathymetry compared to the Point Arena–Point Reyes section of Region A (i.e., Monterey Bay and the Channel Island region south of Point Conception). It has, however, only a few persistent upwelling centers (e.g., Point Sur). Region C is off Baja California (Figure 1d), has complex bathymetry, especially near Punta Eugenia, and has several strong upwelling centers.

The images were taken from 1981 to 1990 and included months from March through November (Table 1). A total of 15 realizations were selected for Region A, 16 for Region B, and 13 for Region C. Hereinafter, individual images are referred to by name (e.g., A12); A for region A and 12 for the 12th image in the given chronological sequence. Pass identification for each image also is given in Table 1. Images from Region A were centered at 38°N, 125°W, those from Region B at 35°N, 122°W, and those from Region C at 26°N, 115°W. Each image is 512 × 512 pixels. This database was constructed for months (Fig. 2) where past mean wind conditions indicated that strong upwelling occurred (e.g., positive Bakun upwelling index; Bakun, 1973). This search criterion was used because the focus of this study was frontal structure associated with recurrent mesoscale filaments. Generally, these are found in satellite data off the west coast of the United States during periods of coastal upwelling. In addition, images were selected to insure a cloud-free surface area, a necessity when employing objective edge detection methods (e.g., Simpson, 1990).

Data also were selected to insure that each image gave a statistically independent realization of filament structure in the California Current System. Selection criteria used to insure this latter requirement were: 1)

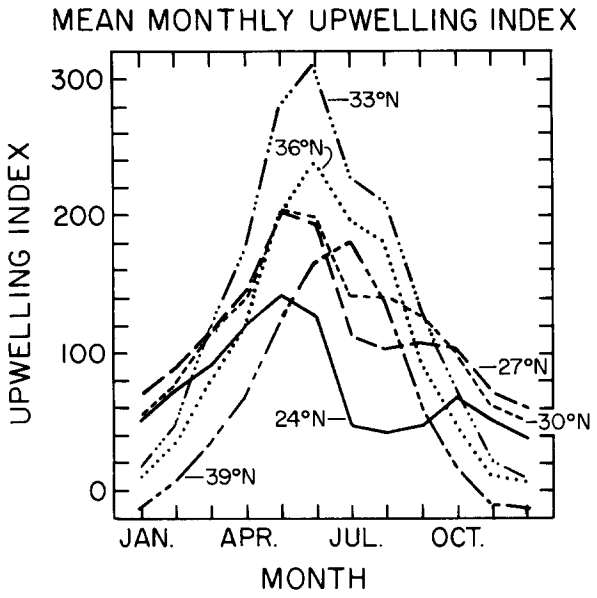

Figure 2. Mean monthly upwelling indices for two different locations within each of the study areas shown in Figure 1. Mean monthly values were computed over a 21-year average from daily upwelling indices. Positive upwelling index provides a measure of the strength of coastal upwelling (Bakun, 1973). Negative indices indicate that downwelling, not upwelling, is occurring near the coast. Region A is characterized by data for latitudes of 39°N and 36°N, Region B by values at 33°N and 30°N, and Region C by values at 27°N and 24°N.

low correlations between the members of temporal sequences of AVHRR images, consistent with the known facts that correlations can significantly drop after 1 day (Wahl and Simpson, 1990), are strongly affected by air–sea exchange processes (Wahl and Simpson, 1990), and are dependent on the seasonal strength of the flow field (Kelly, 1983; Thomas and Emery, 1988); 2) substantial changes are known to occur in the dynamics and orientation of filaments on a time scale of several weeks (Mooers and Robinson, 1984; Rienecker et al., 1985; Dewer et al., 1991). Thus, sampling cloud-free data, separated in time by about a month or longer, provided the best available independent realizations of filament structure. In fact, dates for the images (Table 1) show that, in general, images were separated in time by periods greater than 1 month.

Image Preprocessing

Preliminary processing of the data included earth location and removal of instrument attitude and orbital variations (e.g., Legeckis and Pritchard, 1976), calibration of the 3.7 μm and 11 μm channels (Lauritson et al., 1979 and updates), and registration of the 1.1 km data to the grids of the specific study areas (Fig. 1). Daytime images were cloud-masked using the local dynamic threshold nonlinear Rayleigh (LDTNLR) cloud-masking algorithm (Simpson and Humphrey, 1990). Nighttime images were cloud-masked using the principal component transformation split-and-merge clustering (PCTSMC) algorithm (Gallaudet and Simpson, 1991). Land was masked using a recursive polygon fill procedure with the coast as a boundary (Simpson, 1992). Preprocessing produced a set of cloud- and land-masked IR images for each study region; these are the images used for detailed analysis in this study (Table 1). Hereinafter, they are referred to as primary images.

METHODS

Gradient Calculation

The two-dimensional gradient is defined as

$$\vec{\nabla}\varphi = \frac{\partial \varphi}{\partial x}\hat{i} + \frac{\partial \varphi}{\partial y}\hat{j}, \tag{1}$$

Table 1. Images, Grouped by Region (Fig. 1a), Used in This Study

Region A			*Region B*			*Region C*		
Name	*Date*	*Passid*	*Name*	*Date*	*Passid*	*Name*	*Date*	*Passid*
A1	June 15, 1981	noa681166034100	B1	June 11, 1981	noa681162215500	C1	Oct 2, 1982	noa782275220300
A2	July 8, 1981	noa681189031600	B2	Oct 16, 1981	noa781289221900	C2	April 2, 1983	noa783092221500
A3	Sept 30, 1981	noa781273220200	B3	Aug 5, 1982	noa782217215300	C3	May 3, 1983	noa783123224100
A4	July 14, 1982	noa782195225400	B4	Oct 8, 1982	noa782281223300	C4	Aug 14, 1985	noa985226551130
A5	May 19, 1983	noa783139224830	B5	July 14, 1983	noa783195231000	C5	Nov 2, 1985	noa985306212330
A6	July 15, 1983	noa783196225800	B6	Oct 4, 1983	noa783277231530	C6	Sept 15, 1985	noa985252214230
A7	Sept 12, 1983	noa783255224245	B7	May 10, 1984	noa784131234521	C7	July 19, 1986	noa986200221045
A8	July 7, 1984	noa784189233600	B8	June 29, 1984	noa784181233400	C8	March 27, 1987	noa987186223100
A9	Aug 7, 1984	noa784220123430	B9	July 25, 1984	noa784207231500	C9	Sept 9, 1987	noa987252225130
A10	Sept 11, 1984	noa784255232400	B10	Sept 1, 1984	noa784245234730	C10	May 24, 1989	noab89144210200
A11	May 5, 1987	noa987122030220	B11	July 8, 1985	noa985189220330	C11	June 30, 1989	noab89181212400
A12	July 31, 1987	noa987212232140	B12	April 20, 1987	noa987110231400	C12	July 30, 1989	noab89211211540
A13	June 27, 1988	noa988179234600	B13	Oct 4, 1987	noa987277232400	C13	June 14, 1990	noab90165213910
A14	July 16, 1988	noa988199233100	B14	June 29, 1988	noaa88181025730			
A15	Oct 17, 1988	noa988291233200	B15	July 5, 1989	noaa89186160200			
			B16	June 4, 1990	noab90165213910			

where $\varphi(x,y)$ is the SST distribution of an image. The direction of the edge is determined by the relation

$$\theta = \arctan\left[\frac{\partial\varphi / \partial y}{\partial\varphi / \partial x}\right] \tag{2}$$

and the gradient magnitude is defined as

$$|\vec{\nabla}\varphi| = \left[\left(\frac{\partial\varphi}{\partial x}\right)^2 + \left(\frac{\partial\varphi}{\partial y}\right)^2\right]^{1/2}. \tag{3}$$

A 3×3 isotropic gradient operator (Jain, 1989) was convolved with the input image; every cloud-free ocean pixel served as a center for these filter operations. The isotropic gradient operator was chosen because of its good edge detection characteristics when used with AVHRR images as compared with other nonstochastic edge detectors (Simpson, 1990). The operator computes a centered finite difference approximation to the thermal gradient in two orthogonal directions ($\Delta T / \Delta x$), $\Delta T / \Delta y$) as described in Simpson (1990). A two-banded image of SST gradient angle and magnitude was computed for each image in Table 1 using Eqs. (2) and (3). If a zero (reserved for cloud and / or land masked pixels) was encountered anywhere in the 3×3 input image tile or in a one pixel radius around the tile, then the value of the gradient was rejected and zeros placed in both bands of the derived gradient image. This was done to avoid calculating erroneous gradients at ocean-cloud or ocean-land boundaries.

In this study, $\vec{\nabla}\varphi$ is defined such that its unit normal points in the direction that maximizes temperature gradient. A positive gradient is defined to be gradient measured from low to high temperatures. The gradient angle is defined as the clockwise rotation from a vertical line due south of the pixel in question through the unit normal of $\vec{\nabla}\varphi$ described above. Figure 3a shows the range of gradient angles assigned according to the aforementioned conventions for the boundary between a circular parcel of warm water and cool surrounding water. Because the value 0 is reserved for cloud and / or land masked pixels, a north–south edge with cold water to the north and warm water to the south is assigned to an angle of 360°. Likewise, an edge with warm water to the north and cold water to the south is assigned to an angle of 180°. Figure 3b shows examples of gradient angles at various edges of a hypothetical filament using the previously defined angular conventions.

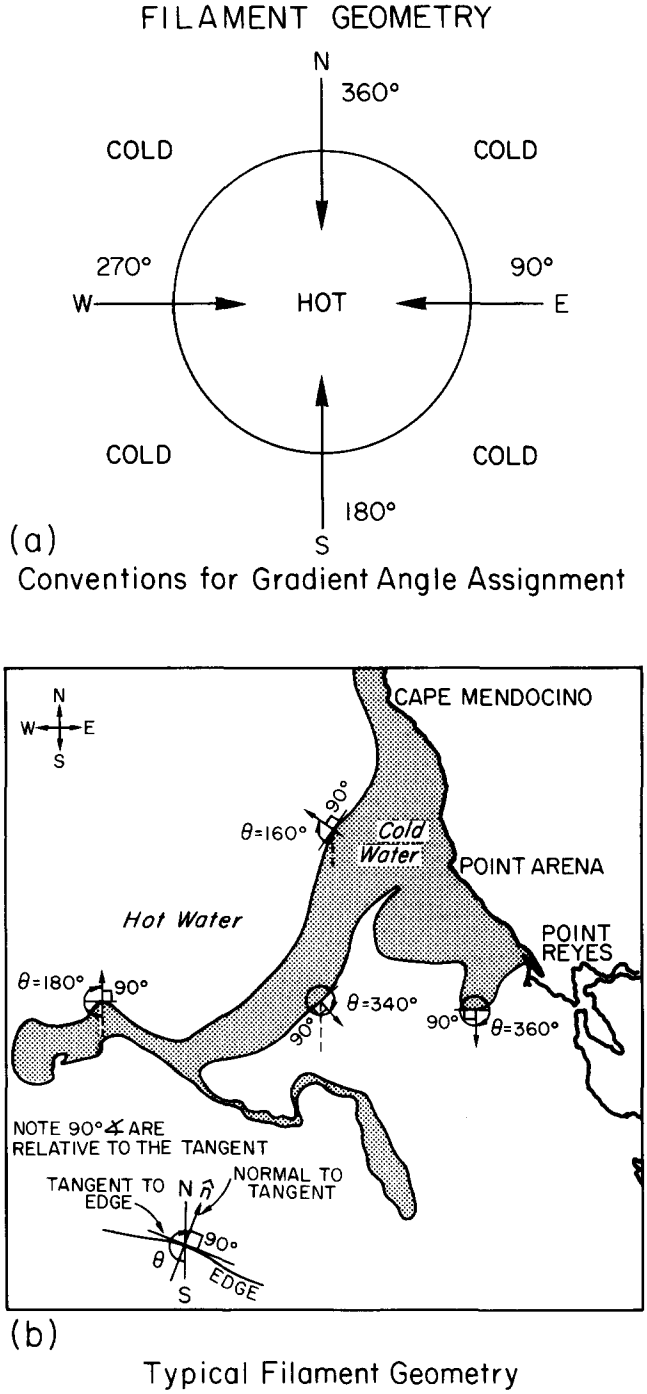

Figure 3. a) Diagram showing the range of gradient angles [Eq. (2)] assigned according to the conventions defined in the text for an edge separating a circular parcel of warm water from cooler surrounding water. Application of this convention to the hypothetical filament shown in b). Note the angle θ is measured from the direction of true south and the normal vector $\hat{n}$ is perpendicular to the local tangent as shown in the figure insert.

Gradient Resolution and Error

The spatial resolution of AVHRR at nadir is 1.1 km per pixel. Thus, the ΔX and ΔY computed using Eq. (3) have their smallest value (2.2 km) for tiles located close to nadir viewing. If the spatial rate of change in SST remains constant over a minimum distance of 2.2 km, then the isotropic operator yields spatially accurate estimates of gradient. When changes occur over a spatial scale less than 2.2 km, however, then the edge detector tends to smooth out the edge and the strength of the gradient is underestimated. While the spatial scale of s-type boundaries reported in the literature cannot be

resolved fully with AVHRR data, it is possible to differentiate filament boundary types with this data using accurate edge detection methods. Other gradient operators, including the simple 2 × 2 Roberts operator, would have provided greater spatial resolution at the cost of significant noise amplification and erroneous edge detection (Simpson, 1990).

Two other sources of error that often can be minimized also contribute to poor gradient estimation. The first of these occurs when $\vec{\nabla}\varphi$ (in this case ΔT) is incorrectly calculated. The most common cause of this error is a failure to properly mask all cloud and land pixels from the image prior to gradient analysis. Thus, effective cloud- and land-masking algorithms (e.g., Simpson and Humphrey, 1990; Gallaudet and Simpson, 1991; Simpson, 1992) are essential preprocessing steps when accurate SST gradients are needed. Another major source of error in ΔT is sensor noise (e.g., time varying calibrations associated with aging satellite electronics and data dropouts associated with degraded beam transmission / reception). Images that suffered from problems of this nature were excluded from the study.

The other source of avoidable error lies in the calculation of the denominator, ΔX and ΔY, of Eq. (3). Pixels with viewing angles far from nadir are assigned a larger surface area than those at nadir. This can result in either a positive or negative error in gradient magnitude, depending on the location of thermal features relative to off nadir pixels in the image. Gradient angles computed using Eq. (2) are similarly affected. To minimize problems associated with this effect, edge passes were not used in the study because such passes accentuate off-nadir pixel distortion (e.g., Legeckis and Pritchard, 1976).

Analysis Procedures

Histograms of gradient magnitude within 0.1°C km^{-1} intervals were made in order to compare gradients strength between regions. These plots (Fig. 4) used all available data for a given region. The two-banded images of gradient magnitude and angle were further processed by a thresholding algorithm that set all cloud-free ocean pixels in both bands equal to zero if the gradient magnitude was less than 0.1°C km^{-1}. This was done to remove small-scale gradients below the sensitivity of the AVHRR sensor and to eliminate sensor noise (Simpson, 1990).

In addition, processing was performed to examine the relations between gradient magnitude and the orientation of the gradient (edge) with respect to the ocean surface. Both the thresholded and the original gradient images were sorted pixel by pixel according to angle, with gradient magnitudes averaged in 5° angular intervals. The resulting distributions (consisting of 72 points per image) were median filtered to remove high-frequency noise. Also, a subset of three images for each

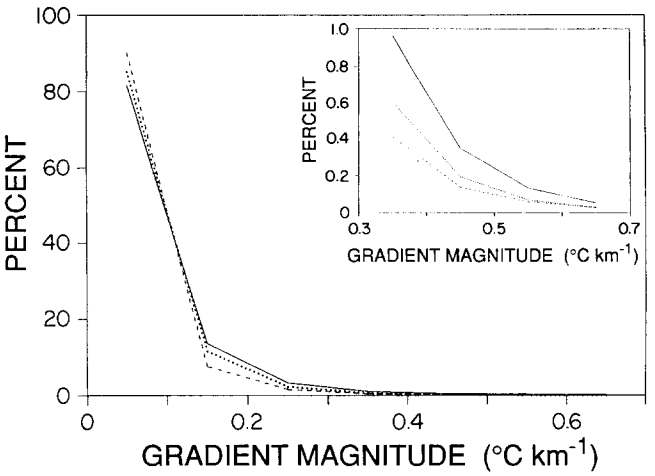

Figure 4. Mean plots, by region (Fig. 1), of percent of pixels as a function of gradient magnitude for the images listed in Table 1. Solid, dotted, and dashed lines denote curves for regions A, B, and C, respectively.

study area was formed and distributions of gradient magnitude vs. angle were made using gradient thresholds of 0.0°C km^{-1}, 0.05°C km^{-1}, 0.10°C km^{-1}, 0.15°C km^{-1}, and 0.20°C km^{-1}. The images used in this particular analysis were A1, A3, A14, B8, B10, B11, C2, C5, and C10. The purpose of this analysis was to examine variations in the distribution of gradient structure as a function of noise threshold.

Principal Component Analysis

A principal component transformation (PCT) was performed on the 44 distributions of gradient magnitude vs. gradient angle computed from the images used in this study. PCT analyses also were performed on the regional subsets of the 44 distributions. The PCT is useful for compressing the dimensionality of data sets into a few major representative patterns. The PCT has a broad theoretical and practical background (Hotelling, 1933; Okamato, 1969; Richman, 1986; Preisendorfer, 1988; Gallaudet and Simpson, 1991; 1993); thus, only a brief description of the PCT as it relates specifically to this analysis is presented below. The following description is given with respect to the entire data set. Regional analyses were identical, with the exception that instead of using 44 distributions, sets of 15, 16, and 13 distributions were used for Regions A, B, and C, respectively.

Forty-four gradient magnitude vs. gradient angle distributions were computed as described above. Each distribution consists of 72 points with mean gradient value for each 5° interval of gradient angle. The entire data set can be treated as a 44 × 72 data matrix, **X**. Each row of **X**, denoted $[\boldsymbol{x}_i]$, represents the gradient magnitude vs. gradient angle distribution for a given image. Each column of **X**, denoted $\boldsymbol{x}_j$, represents one of the 72 angular intervals of mean gradient. Define the 44 × 1 angular mean column vector $\boldsymbol{m}_x$, as

$$m_x = \frac{1}{N}\sum_{j=1}^{N} x_j, \tag{4}$$

where N is equal to 72, for the 72 angular intervals of mean gradient that comprise the columns of **X**. The covariance matrix, C_x, of the data array **X** is (e.g., Jain, 1989):

$$C_x = \frac{1}{N-1}\sum_{j=1}^{N}(x_j - m_x)(x_j - m_x)^T = \frac{1}{N-1}X'X'^T. \tag{5}$$

In this form, C_x is a 44×44 real, symmetric matrix. Note that m_x is removed from each column x_j in **X** to form the demeaned-array X' from which C_x is constructed using (5). Thus, each of the diagonal elements of C_x represents the variance in the ith row of **X**. The off-diagonal elements of this matrix contain the covariance between the gradient magnitude vs. gradient angle distributions for different pairs of images in the set of 44 images.

The principal component transformation is a linear transformation such that

$$Y = GX, \tag{6}$$

subject to the constraint that the off-diagonal elements of the covariance matrix of the data set **Y** are zero (Richards, 1986). Thus, the PCT forces the rows of **Y**, denoted $[y_i]$, to be completely uncorrelated. The transformed covariance matrix, C_y, simply is

$$C_y = \frac{1}{N-1}\sum_{j=1}^{N}(y_j - m_y)(y_j - m_y)^T, \tag{7}$$

where y_j and m_y have been formed from x_j and m_x using Eq. (6). The matrices C_y, C_x, and **G** satisfy the eigenvalue equation

$$\mathbf{G}^T C_y = C_x \mathbf{G}^T, \tag{8}$$

where C_y is the diagonal matrix of eigenvalues of C_x, and **G** is the transpose of the matrix of eigenvectors of C_x, provided that **G** is orthonormal. Thus, Eq. (8) can be rewritten as

$$C_x g_n = \lambda_n g_n, \tag{9}$$

where the subscript n referes to the nth eigenvector–eigenvalue pair. **G** is found by solving for the eigenvectors of C_x; it is dimensionless. Because the PCT is a linear transformation, the **Y** data matrix remains in the same units as **X**, which in this case is °C km^{-1}.

The rows of the transformed data **Y**, denoted $[y_i]$, are uncorrelated and are known as the principal components of **X**. They are ordered so as to contain a successively decreasing amount of variance (Ingerbritsen and Lyon, 1985). The transposed eigenvectors of C_x are the rows of **G**. These eigenvectors indicate the weighted contribution of columns in **X** (i.e., the angular intervals of **X**) to each principal component or row of **Y**. There is one eigenvector for each principal component; an eigenvector is multiplied with each of the 72 angular intervals of **X** separately to generate the 72 angular intervals of the corresponding principal component. The corresponding eigenvalues, λ_n (i.e., the diagonal elements of C_y) represent the variance contained in each row of **Y**. When the PCT compresses the representation of a given data set **X**, then the first few rows of **Y** contain most of the original variance. If this condition holds for the derived distributions of gradient magnitude vs. gradient angle, then the first few rows of **Y** will contain the dominant angular patterns that contribute most of the variance found in the 44 gradient distributions.

RESULTS

Imagery

Space precludes presenting figures for each of the 44 images analyzed as a part of this study. Hence, only representative results, consisting of a primary image and derived products from each study region, are included in this article. The following conventions apply to each of the three figures (i.e., Figures 5, 7, 8). For all panels in these figures, clouds, land, and data not in the grid are masked in black (pixels equal to zero); coastlines are shown with dotted white lines. Panel a) is a calibrated SST map constructed from AVHRR Band 4. Each of these images was individually contrast stretched (hence has a different temperature wedge) to optimize visualization of the thermal structure in a given image. Very dark or grey shades represent cold, inshore coastal water; lighter shades represent warmer offshore California Current water. Wedge units are in °C. Panel b) is a map of gradient angle computed using Eq. (2) with the directional conventions shown in Figure 3. Wedge units are given in degrees of the compass. Panel c) shows the magnitude of the SST gradient computed using Eq. (3) with a 3×3 isotropic gradient operator. The wedge has units of °C km^{-1}. Panel d) shows the thresholded magnitude of the SST gradient [i.e., all temperature gradients < 0.1 °C km^{-1} were deleted from the data to eliminate high frequency noise (e.g., Simpson, 1990)]. Name places cited in the presentation of results are marked clearly in the reference grids of each region (Fig. 1); to avoid cluttering of the images, these name places are not repeated in Figures 5–8. The descriptions given below are based solely upon the images used in this article (Table 1). These conditions may not prevail at all times in these regions (e.g., the winter season in which winds predominantly but not exclusively are downwelling favorable, and during periods of intense cloud cover representative of different meteorological conditions).

Region A

Realizations from Region A are characterized by cold, upwelled water present along the entire coast of the study area. Persistent sites of filament generation are

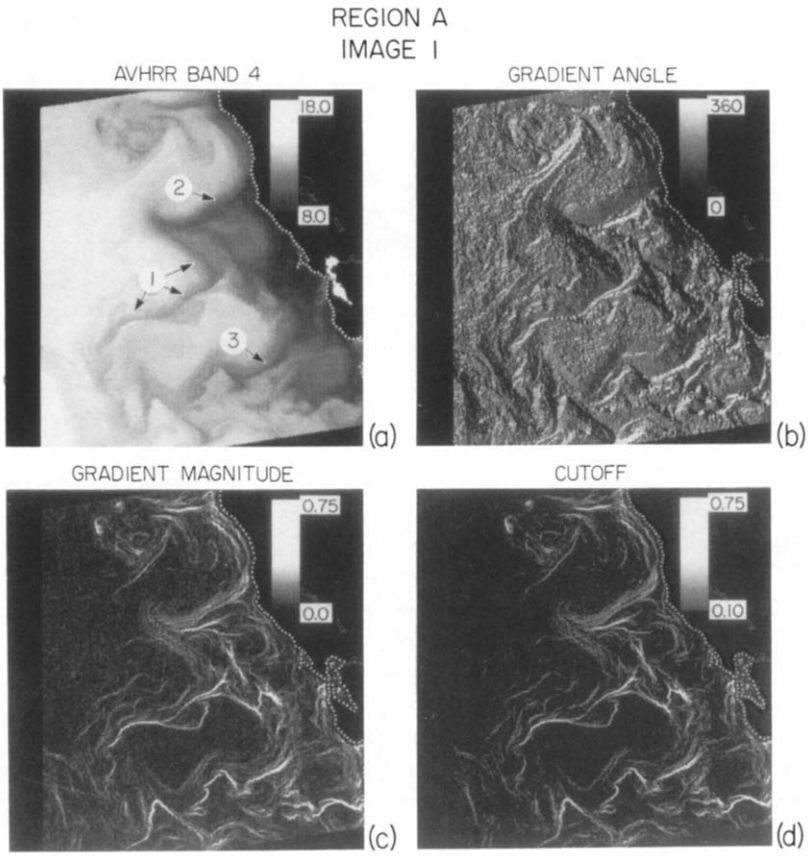

Figure 5. Region A, Image A1: a) AVHRR Band 4 sea surface temperature (°C); b) image of gradient angle computed using Eq. (2) in units of degree of the compass (Fig. 3); c) image of gradient magnitude (°C km^{-1}) computed using the isotropic gradient operator; d) a thresholded version of c) with all values below the cutoff value of 0.1°C km^{-1} removed.

Cape Mendicino and Point Arena. Filaments sometimes appear directly offshore of one of these upwelling centers. More frequently, however, near the coast the cold water jets are oriented southward. At promontories to the south, the filaments often appear further offshore. Filaments from this region are typically narrow and extend offshore at near right angles to the coast. Temperature statistics (Table 2) and histogram information on the magnitude of the gradients in these images (Fig. 4) provide an overall description of gradient strength for Region A.

In Figure 5a, a filament projects into the California Current off Point Reyes (arrow 1). The origin of the water appears to be further north near Point Arena (arrow 2) and not Point Reyes. These data imply that water was drawn offshore at Point Arena, doubled back between Point Arena and Point Reyes, and finally moved farther offshore into the California Current adjacent to Point Reyes. The overall filament configuration has the shape of a backwards letter "Z." Another filament (arrow 3) is visible further south, possibly associated with upwelling that occurred south of Point Reyes.

Figure 6a shows a colored version of Figure 5d. The white box in this panel identifies a region of this image which was zoomed (Fig. 6b) to examine the details of the filament geometry. The s-type boundary in Figure 6b is denoted by intense gradients (indicated by the color blue and arrow 1) occurring over a distance of a few kilometers. The d-type edge has much weaker gradients (indicated by white and yellow pixels and arrow 4) and is significantly wider. Arrow 3 shows a splinter off the main s-type boundary of the filament. Arrows 2 and 5 denote the s-type and d-type boundaries of what may be a feeder into the larger filament.

Region B

Realizations from Region B do not exhibit the narrow jetlike structure common to filaments found in Region A. Filaments, when they do exist, are often wider and more poorly defined compared to those in Region A. Filament orientation (e.g., Fig. 7) seems to occur at angles less than 90° relative to the coast, and in many instances sections of filaments appear parallel to the coast. In most images, cold water occurs close to shore off Monterey and south along central California, although accompanying filament structure is less frequent. The Southern California Bight and Channel Island region, visible in the lower right hand corner of Figure 7, shows a high degree of surface temperature variability and complex gradient structure. This structure, however, probably is not upwelling-related because the SST in this area is relatively high. In this region, the California Current splits; one branch turns east and circles north as part of a semipermanent cyclonic eddy (i.e.,

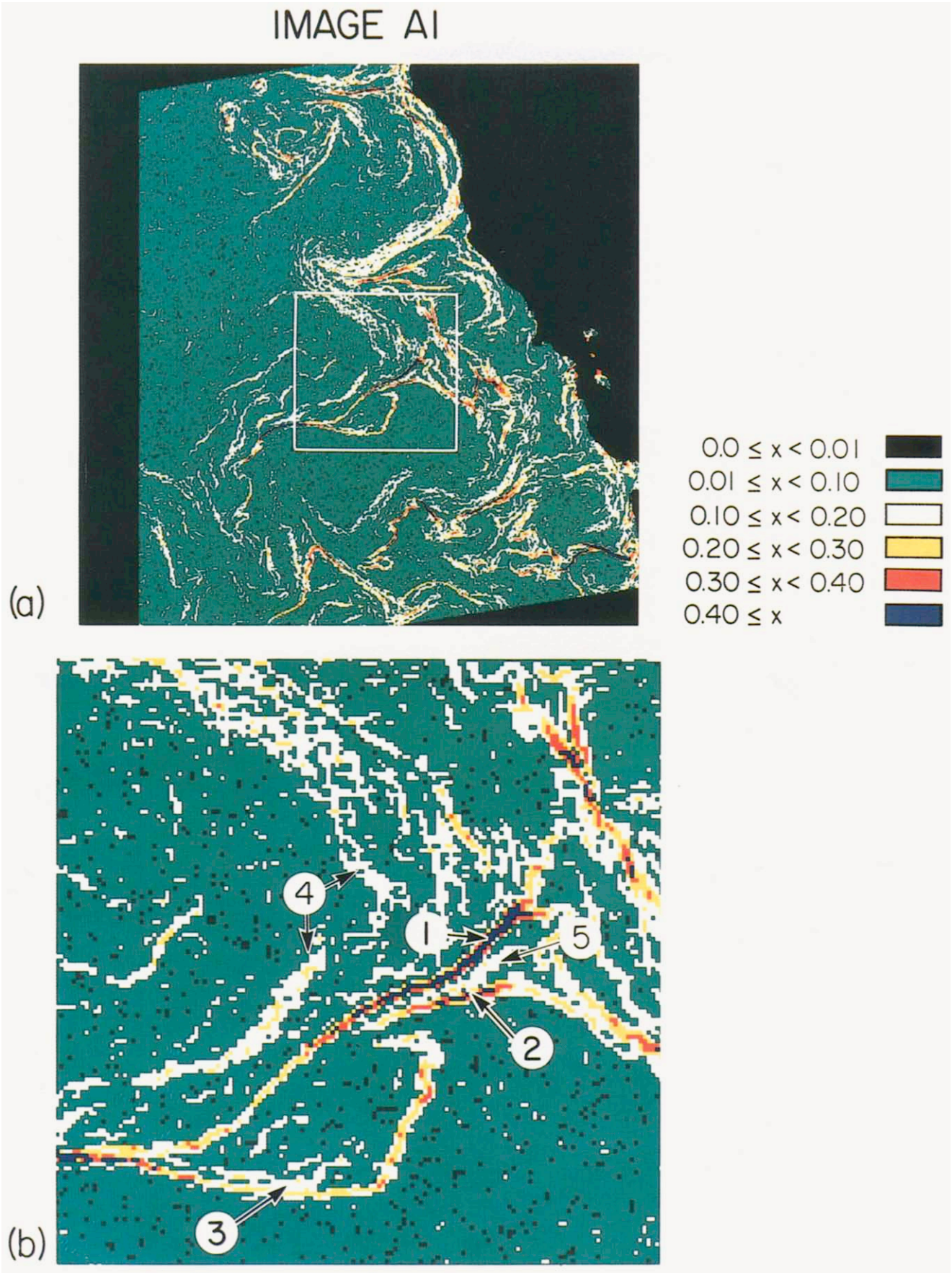

Figure 6. Colored version of Figure 5d. The white box denotes the area zoomed and displayed below. b) Expanded view of the area in a) defined by the white box. The northern boundary 4, and the southern boundary 1 of the major filament in this section of the image are highlighted. Feature 3 is a return branch of the main filament. Arrows 5 and 2 refer to the d-type and s-type boundaries of a feeder filament, respectively.

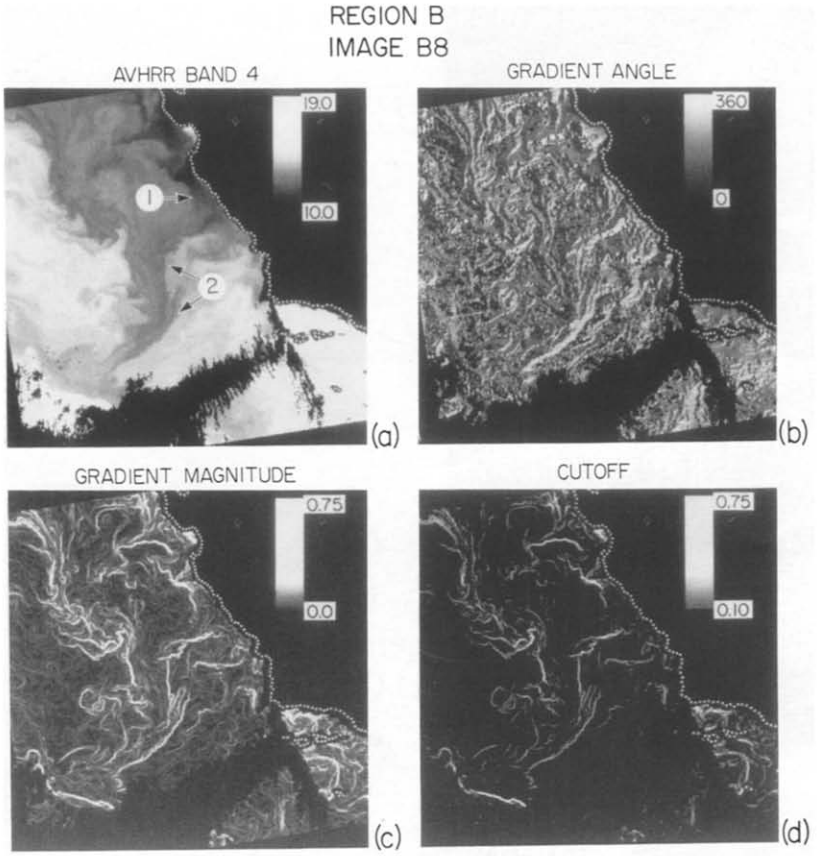

Figure 7. Analogous to Figure 5, except for Region B, Image B8.

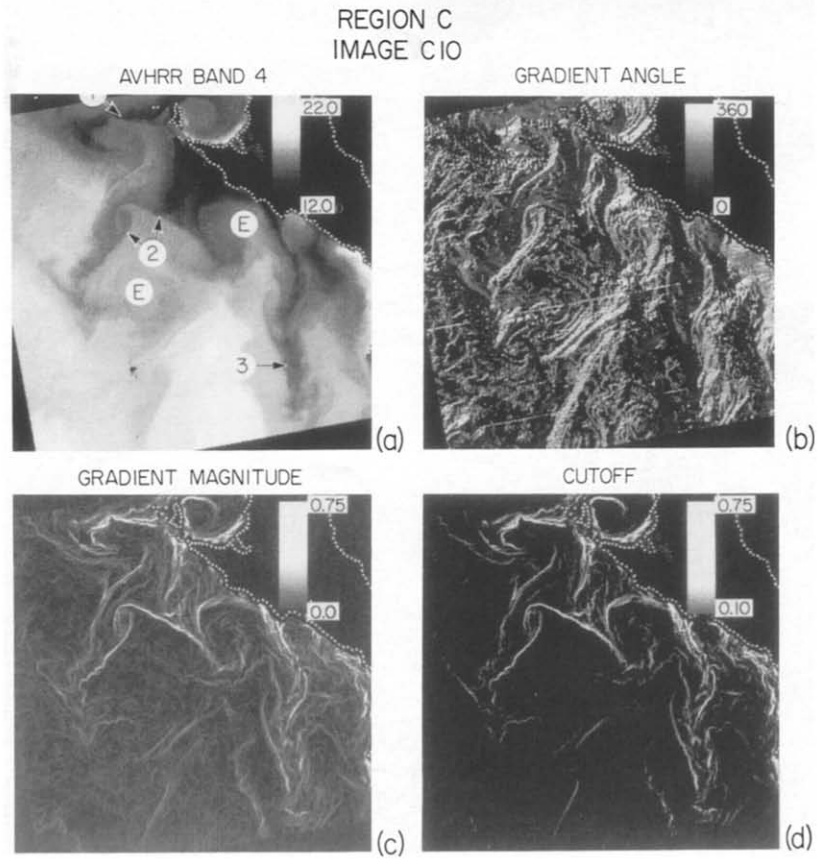

Figure 8. Analogous to Figure 5, except for Region C, Image C10. The inshore E indicates the surface signature of an inshore cyclonic eddy. The offshore E indicates the possible surface signature of a weaker cyclonic eddy.

Table 2. Statistical Summary of the Temperature Information Contained in Each Image by Region[a]

Region A					*Region B*					*Region C*				
Name	T_{min}	T_{max}	T_{mean}	T_{stdev}	*Name*	T_{min}	T_{max}	T_{mean}	T_{stdev}	*Name*	T_{min}	T_{max}	T_{mean}	T_{stdev}
A1	7.723	18.731	12.596	1.518	B1	9.948	16.167	12.985	0.910	C1	16.601	26.081	20.528	1.237
A2	7.938	22.467	12.525	1.334	B2	6.756	21.594	14.988	1.046	C2	14.907	22.635	17.768	1.192
A3	9.607	20.147	14.088	1.454	B3	10.929	17.409	13.922	0.930	C3	13.198	19.107	17.178	0.992
A4	9.463	19.515	13.685	1.075	B4	10.612	18.774	14.815	1.133	C4	14.817	23.007	19.991	1.164
A5	8.750	16.346	12.443	0.994	B5	11.516	18.964	14.932	1.034	C5	16.283	24.324	20.612	1.136
A6	8.584	17.060	13.159	1.200	B6	14.911	17.843	16.397	0.423	C6	16.736	23.417	20.059	1.029
A7	11.858	21.096	15.888	0.789	B7	7.427	16.816	12.055	1.155	C7	13.895	24.233	19.565	1.390
A8	9.047	15.820	13.225	1.070	B8	9.895	19.108	13.636	1.266	C8	12.152	18.556	16.006	1.028
A9	8.877	20.389	14.198	1.136	B9	13.118	22.082	15.943	1.293	C9	18.830	27.174	22.199	1.368
A10	9.350	19.410	14.192	1.231	B10	12.058	21.507	16.596	1.182	C10	12.141	21.591	16.959	1.179
A11	5.314	23.074	12.646	0.677	B11	10.757	21.793	16.381	1.297	C11	13.446	20.318	17.539	0.867
A12	9.730	18.204	14.273	1.177	B12	10.143	15.909	13.277	0.973	C12	15.424	22.298	19.494	0.811
A13	8.195	15.091	13.018	1.195	B13	12.562	22.438	16.746	1.522	C13	13.699	18.636	16.738	0.816
A14	9.548	18.158	14.909	1.569	B14	9.314	20.560	13.814	1.279					
A15	10.634	24.863	14.799	1.170	B15	9.834	18.335	13.950	0.967					
					B16	9.051	18.420	13.590	1.159					

[a] T_{min}, T_{max}, and T_{mean} are the minimum, maximum, and mean temperature for each image. T_{stdev} is the standard deviation about the mean temperature.

Southern California Eddy) centered around the Channel Islands and outer banks (e.g., Hickey, 1979; Lynn and Simpson, 1987). This branching flow, not upwelling, causes the complex SST gradients observed in the Southern California Bight sections of the images for Region B. Temperature statistics (Table 2) for images in Region B and a histogram of the thermal gradients magnitude in these images (Fig. 4) provide an overview of filament strength for the region.

A wide filament with an origin near the coast south of Monterey (Fig. 7 and arrow 1) appears with a southward orientation adjacent to the central California coast. Further south, it appears farther offshore. While the s-type edge (arrow 2) of this filament is visible (Figs. 7b, c, d), it is much weaker than the s-type boundaries associated with filaments in Region A [remember that each image (Figs. 5, 7, 8) was individually contrast-stretched for optimal visualization]. This filament appears to have a disjoint frontal structure. The d-type edge of this filament (Fig. 7d) is very diffuse in places, making it difficult, at times, even to recognize. This is consistent with the generally weaker edge structure observed for filaments in Region B compared to Region A (also see Fig. 4).

Region C

Upwelling in Region C occurs at the northern most tip of Punta Eugenia and south along the coast. SST generally increases offshore and to the south, consistent with large-scale climatological observations (e.g., Robinson, 1976; Lynn et al., 1982). Most images for Region C have large offshore regions with temperatures well above 20°C. While filaments are visible in Region C, frontal structure often is composed of discontinuous edges which appear separated from upwelling sources. Filaments off the northern tip of Punta Eugenia often occur with either a westward or southwest orientation. Filaments associated with promontories further south along the coast frequently are oriented south or southwest. Typically, warm water is found on the upper portion of Punta Eugenia near Scammon Lagoon. This gives rise to the large temperature gradients generally found in this area which are not associated with coastal upwelling. Temperature statistics (Table 2) and a histogram (Fig. 4) of gradient strength in these images provide a summary of the imagery for Region C.

Three filaments (arrows 1, 2, and 3) branching out from the cold upwelling water found along the coast are shown in Figure 8. Consistent with climatology for the region, warm water dominates the southern portion of this image. Here, some of the most intense filament boundaries have a north–south orientation (Fig. 8d). There also is evidence of strong cyclonic eddy formation near the coast in the sea surface temperature pattern (Fig. 8, E near coast) and a possible weaker cyclonic eddy farther offshore (Fig. 8, E farther offshore).

Occasionally, very low level quasiperiodic noise can occur in AVHRR thermal data and usually cannot be detected visually (e.g., Fig. 8a). Gradient enhancement techniques can amplify this noise (i.e., the periodic line segments shown in Fig. 8b). The precise reason for this instrumentation noise is unclear. We have established, however, that this noise is not an artifact of the analysis procedures. Moreover, it has no impact on the results and conclusions presented.

Regional Differences in Gradient Strength

Histograms of the 44 images of gradient magnitude provide information on the relative strength of thermal

gradients for the three regions sampled. The histograms for all three regions are exponential in nature (Fig. 4). Region A, denoted by a solid line, has the smallest percentage of pixels in the 0–0.1°C km^{-1} interval and the largest percentage of pixels with the strongest thermal gradient (≥ 0.4°C km^{-1}). Region B, denoted by a dotted line, has a higher percentage of pixels in the 0–0.1°C km^{-1} interval than region A and has fewer pixels with strong thermal gradients. Overall, Region C, denoted by a dashed line, has the weakest thermal gradients of the three regions. The data used to compute the histograms in Figure 4 consists of about 10^6 gradient estimates per region.

Distributions of Gradient Magnitude as a Function of Gradient Angle

Distributions of gradient magnitude vs. gradient angle provide a more compact representation of the gradient information contained in each image. Each gradient pixel within an image is weighted equally. Thus, these distributions can be used only to determine the statistical characteristics of fronts within a region because, in this representation, the spatial relation between individual frontal segments (i.e., pixels) is lost.

A surface pattern with a random orientation of gradients (e.g., an image of gaussian noise or an image of SST produced by random ocean mixing) would have a horizontally uniform distribution of gradient strength as a function of angle. Analysis of images of gaussian noise (not shown) confirm this expected distribution. Deviations from this uniform distribution for images of oceanic SST indicate that mean gradient strength changes with edge orientation.

Region A

The mean distribution of gradient magnitude vs. gradient angle for all images from Region A has maximum gradients near 0°, drops to a minimum near 160° and then slopes upward again to maximum near 360° (Fig. 9a). Note that 0° and 360° are the same point in these distributions, and thus there is only one maximum. The minimum and maximum gradient values of the distribution are about 180° out of phase. The distribution is symmetric around the minimum.

Region B

The mean distribution for all images from Region B drops from high gradients near 0° to minimum gradients near 140° and then sharply rises to maximum gradient values between 200° and 300° (Fig. 9b). The minimum and maximum gradients are separated by roughly 90°. Also, the mean distribution is not symmetric about its minimum.

Region C

The mean distribution for Region C has maximum gradients near 0°, gradually drops to a broad minimum between 120° and 160° and then slopes upward to maximum gradient values near 360° (Fig. 9c). The minimum and maximum gradient values are separated by about 180°. The distribution is more symmetric about its minimum than that of Region B but less symmetric than that of Region A.

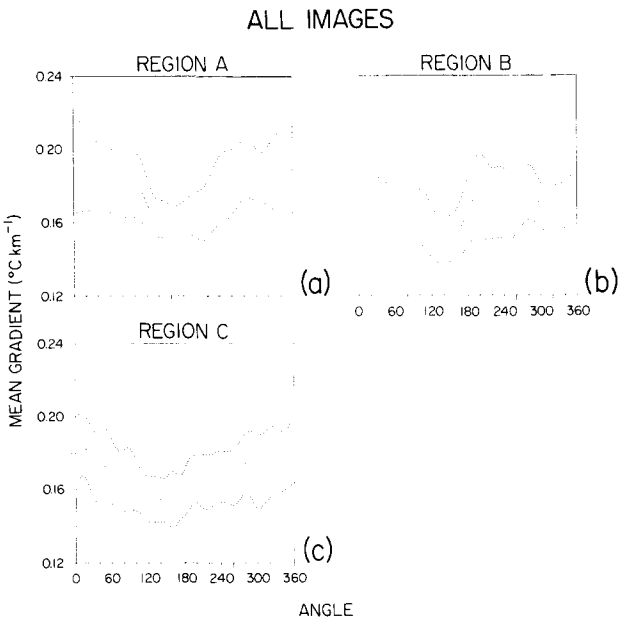

Figure 9. Mean distributions of gradient magnitude vs. gradient angle for the three regions incorporating all images from each region. One standard deviation above and below the mean is given by the dotted curves.

Effects of Thresholding on Distribution Patterns

A subsection of data consisting of three images from each study area was used to determine the effects of different noise thresholds on the mean gradient magnitude vs. gradient angle distributions. An example of the results for image A1 is shown in Figure 10. In this set of figures, the threshold for gradient pixel rejection and subsequent pixel masking increases successively from no threshold in Figure 10a to a threshold of 0.20°C km^{-1} in Figure 10e. For Figures 10a–e, the range in mean gradient (on the vertical axis, the difference between the minimum and maximum) increases in a fashion roughly proportional to the gradient value of the image threshold. This observation was true for all the images examined in the study. Thus, as more pixels with weaker gradients are excluded from an image with higher thresholds, the weaker d-type filament boundaries are systematically removed from the distribution, contributing to the increased range seen in the distributions as well as changes in their relative shapes.

Principal Component Analysis of Distribution Patterns

The results from the principal component analysis on the mean gradient magnitude vs. gradient angle distributions

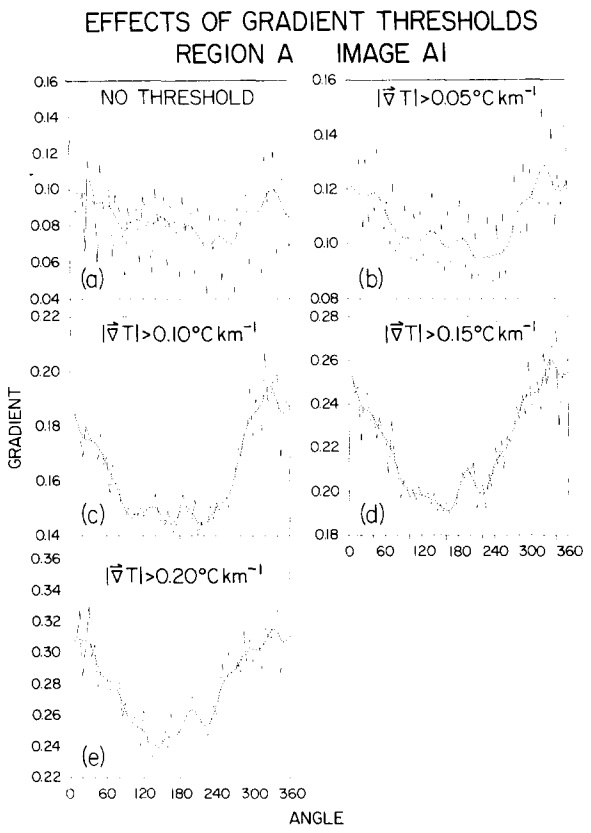

Figure 10. Effects of gradient thresholds on the distribution of mean gradient magnitude vs. gradient angle for a typical image. Thresholds used are indicated in individual panels of the figure.

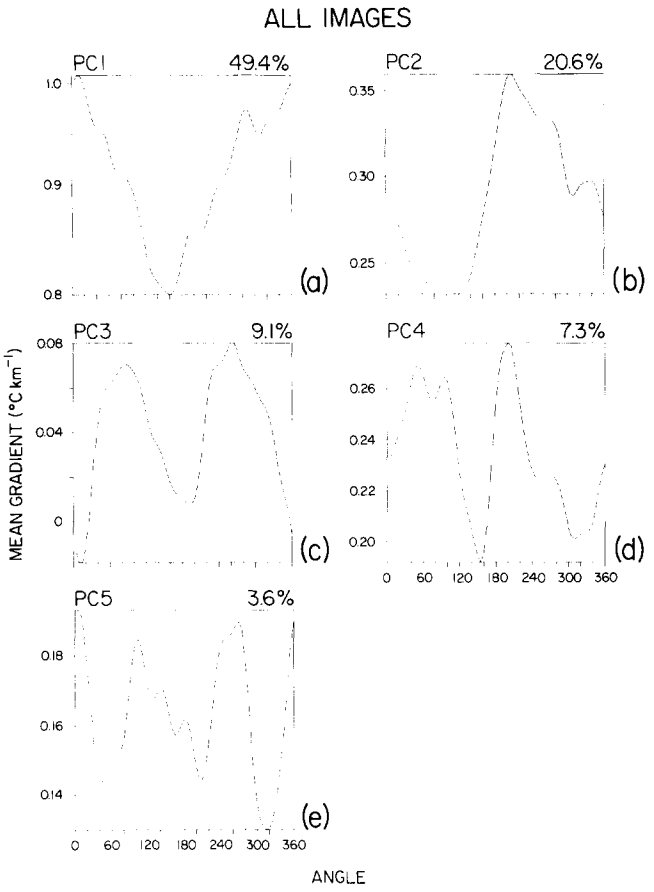

Figure 11. The first five principal components for the complete data set consisting of 44 mean gradient distributions averaged over 5 degrees of compass direction. The percentage value corresponds to the percentage of total variance contained in that principal component.

indicate that the data set was effectively compressed: the first five principal components contained over 90% of the variance. The dominant mode (Fig. 11a) contained 49% of the variance. Examination of the eigenvectors (Fig. 12) shows that images from June–July in Region A and August–November in Region C contributed significantly to this pattern. The second dominant mode (Fig. 11b) contains a sharp transition between 140° and 200° and contains about 21% of the variance. Images that had large positive contributions (Fig. 12b) to this pattern include images from June–July in region B and images from June–November in Region C. This pattern is strikingly similar to the mean distribution for all 16 images in Region B (Fig. 9b). The three other largest dominant modes are shown in Figures 12c, d, and e, respectively. Figure 13 shows the first two principal components for each regional PCT analysis.

DISCUSSION

The Surface Structure of Filaments

Descriptive Synthesis

The transition zone of the California Current system between the offshore oceanic flow and the near shore coastal upwelling region is characterized by large standard deviations and low seasonal ranges in dynamic height (Lynn and Simpson, 1987). Satellite images of the inshore region and transition zone (e.g., Figs. 5–8) contain surface signatures of cold filaments and mesoscale eddies. Complex mixing of inshore and oceanic waters occurs in the transition zone as evidenced by water property distributions (e.g., Simpson et al., 1984; Simpson and Lynn, 1990), as well as chemical distributions (Simpson, 1984) and biological populations (Haury, 1984). Visual interpretation and quantification of thermal fronts in such imagery, however, is difficult because of the overall complexity of the California Current system. The computed distributions (Fig. 9) and PCT results (Figs. 11–13), however, successfully extracted recurrent patterns in the observed frontal structure; each region has a distinct pattern, with one broad directional minima and one broad directional maxima.

The minima in distributions of gradient magnitude vs. gradient angle (Fig. 9) for all three regions were tightly clustered between 120° and 160°, which corresponds to pixels with warmer water to the north / north-

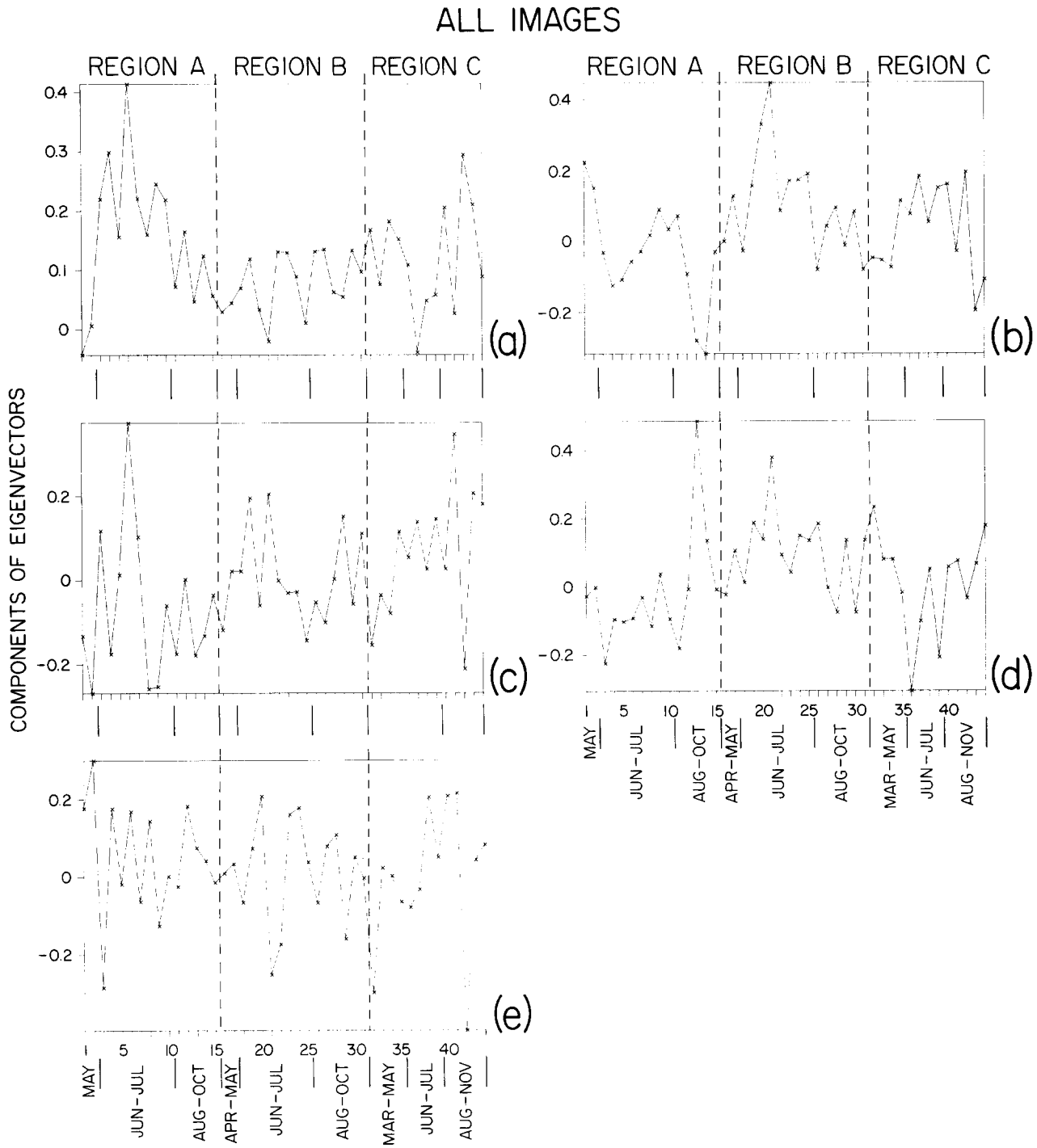

Figure 12. The eigenvectors associated with the principal components shown in Figure 11. Regional and temporal occurrence of a given image also is shown along the *x*-axis of the figure.

west and cooler water the south / southeast based upon the angular conventions adopted in this study (Fig. 3). If such patterns in gradient strength and orientation were not recurrent and / or if they did not contribute significantly to the total frontal structure for a given region, then the distributions of mean gradient as a function of gradient angle (Fig. 9) would have been horizontally uniform, indicative of a random orientation of edge strength. Because these distributions are not uniform and because the data cover a 10-year span with long time gaps between images to insure statistical independence of filament realizations (Table 1), the results from this study provide a more general context for the interpretation of specific in situ frontal observations (e.g., Flament et al., 1985; Rienecker et al., 1985; Simpson, 1985; Strub et al., 1991; Ramp et al., 1991)

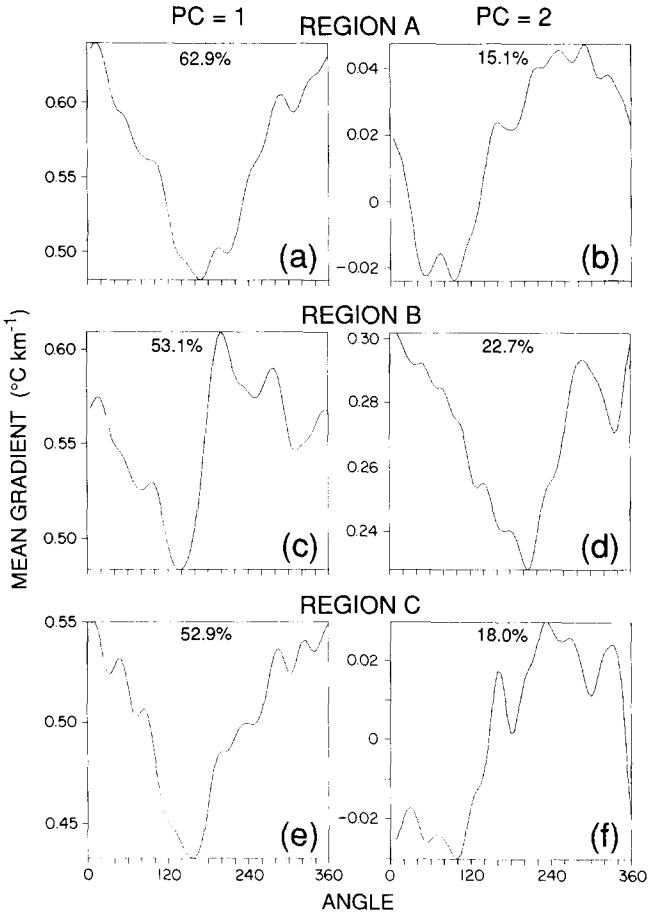

Figure 13. The first two principal components for each of the three regions. Note that the patterns for Regions A and C are reversed from those of Region B, suggesting that the orientation of surface fronts in Region B often are significantly different from those in the other two regions.

in terms of recurrent frontal patterns associated with specific regions of the CCS system.

There are two dominant patterns that represent the majority of the variance in the distributions of mean gradient magnitude vs. gradient angle. The dominant pattern that describes most of the variance of regions A and C is V-shaped with a broad maximum of gradient values near 360° and a minimum near 160° (Figs. 9a and c; also PC1 of regions A and C in Fig. 13). This pattern is consistent with filaments oriented to the west/southwest with s-type and d-type boundaries 180° out of phase. While the results of this study indicate that the sharp/diffuse boundary structure associated with filaments is dominant for regions A and C, it does not necessarily follow that filaments are the only phenomena that exhibit this behavior.

The dominant pattern for Region B has a sharp transition from minimum gradient values near 140° to maximum gradient values near 200° (Fig. 9b; also PC1 of Region B in Fig. 13). This pattern is unlike the dominant pattern from regions A and C and suggests that the thermal frontal structure in region B often is distinctly different from the thermal frontal structure found in regions A and C. This is supported by the principal components analysis (Fig. 13).

The dominant pattern for Region B is similar to the second principal component from regions A and C. The second principal component from Region B is similar to the dominant pattern from regions A and C. This suggests that two distinct types of frontal patterns occur in all three regions, but the relative contribution of one or the other pattern to the total thermal gradient variance varies from region to region.

Analytical Synthesis

The principal component transform of the 44 mean gradient magnitude vs. gradient angle distributions significantly compressed the variance of the original data set. The first five uncorrelated principal components [which are the rows of **Y** in Eq. (6)] account for over 90% of the variance contained in the original data set. The dominant pattern (Fig. 11a) contains almost 50% of the image variance and is strikingly similar to the mean patterns of both Regions A and C (Figs. 9a, c). The second principal component contains about 21% of the variance and is similar in shape to the mean pattern of gradient magnitude vs. gradient angle for Region B (Fig. 9b).

Examination of the eigenvector components (Fig. 12a) associated with the first principal component of **Y** (Fig. 11a, PC1) shows that data from Region A during June–July and from Region C during August–November contributed most of the variance to PC1. Data from Region B contributed relatively little to PC1. The converse, however, is true for PC2 (Fig. 11b). Here the major components of the associated eigenvector are related to data from Region B. With increasing PC number, the PC pattern tends to be less strongly influenced by data from a given region. This is easily seen in PC5 (Fig. 11e) and its associated eigenvector (Fig. 12e); here data from all three regions (A, B, and C) contribute about equally to the variance contained in PC5. The patterns shown in Figures 11 and 12 are further supported by results obtained from the eigenvector analysis performed on a regionally specific basis (Fig. 13).

The first principal component (Figure 11) contains about 50% of the total variance contained in the mean gradient vs. angle distributions (Fig. 9), nearly 2.5 times that contained in the second principal component. This component can be associated with the dominant pattern of thermal gradients found in the images of Regions A and C. This type of structure tends to have maximum mean gradient oriented with warm water to the south and cold water to the north (Figs. 9 and 13). The minimum mean gradients are about 180° out of phase from the maximum mean gradients, with warm water

to the north and cold water to the south. The second principal component (Fig. 11) contains about 21% of the total variance and is almost 2.2 times larger than that contained in the third principal component. This pattern can be associated with frontal structure more characteristic of images for Region B (Figs. 9 and 13). Because about 70% of the total variance associated with the total 10-year data set is contained in these two patterns, it is reasonable to conclude that combinations of these two types of distributions are the predominant thermal frontal structures in the imagery of the California Current used in this study. Again, the relative contribution of one or the other of these two types of patterns to the total thermal gradient variance varies from region to region.

Oceanographic Importance of Filaments in the California Current System

The effects of region-wide recurrent patterns in the frontal structure associated with filaments on two areas of basic and applied oceanography are discussed briefly below.

Acoustic Propagation in the Ocean

Applications of marine acoustics include, but are not limited to, navigation (e.g., Fasham, 1976), fish detection (e.g., Mitson, 1983; Hargreaves, 1975), naval operations (e.g., Jendro et al., 1991; Cheesebrough and Pittenger, 1991), oceanographic variability studies (e.g., Regier, 1982), acoustic telemetry for communications and control (e.g., Cattanach, 1970; Uscinski et al., 1989), and underwater survey (e.g., Roberts, 1971). This diverse set of marine applications has one very important aspect in common: They are all sensitive to variations in sound speed velocity (and hence acoustic index of refraction), which in turn are controlled by the vertical and horizontal distributions of water properties (i.e., temperature, salinity, and pressure), but most especially by temperature (Burdic, 1984).

Both observations and numerical simulations confirm that mesoscale fronts and filaments, such as those identified in this study, are the classic oceanic examples of maximum variation in acoustic propagation characteristics associated with temperature-induced variation in acoustic index of refraction (e.g., Mercer and Booker, 1983; Rousseau et al., 1982; Mellberg et al., 1987; Mellberg et al., 1991) because such regions alter the convergence zone (CZ) characteristics (i.e., relatively narrow regions where rays with differential initial angles return to the surface and near surface ocean; Burdic, 1984). For example, Jendro et al. (1991) constructed sound speed profiles for a California Current filament and then used a range- dependent parabolic equation model to predict sonar ranges in a simulated naval exercise. Their results showed that the acoustic advantage between two adversaries changed as their position relative to the filament and to each other changed because temperature gradients as small as 1°C / 25 km were sufficient to determine whether or not CZ transmission occurs. The typical filament observed in this study has gradients between 0.3°C km^{-1} and 0.7°C km^{-1} at its s-type boundary. Thus, the cold filaments examined herein, and analogous features observed in satellite images of other eastern boundary currents (e.g., Peru Current, Bengula Current), have operational significance. Specifically, the distributions of mean gradient magnitude vs. gradient angle provide quantitative evidence for asymmetric frontal structure in the coastal domain of the California Current System. Thus, the propagation of sound from north to south across d-type and s-type boundaries and on a broader scale across an upwelling region would be likely to behave rather differently if the direction of propagation were reversed. Moreover, because observed frontal structure has regionally specific characteristics (Figs. 9, 11, 12, and 13), it is reasonable to conclude that regional variation in the characteristics of acoustic propagation occurs with the California Current. Thus, it probably is inaccurate to treat the California Current system off the west coast of the United States as a single acoustic province.

Implications of Recurrent Frontal Structure on Biological Distributions and Ecology in the CCS

Laurs et al. (1984) demonstrate that albacore aggregate on the oceanic side of thermal fronts separating clear and warm offshore water from turbid, nutrient rich upwelling water near the coast. In fact, relatively intense fronts seem to be favored in areas offshore of persistent upwelling (Laurs et al., 1977). Their discussion, however, was not framed in terms of the d-type / s-type nature of oceanic fronts in these regions. Because convergence and subduction appears to occur near intense s-type boundaries (e.g., Flament et al., 1985; Ramp et al., 1991), it is possible that albacore orient themselves in order to take advantage of these processes. The subduction process may transport prey out of the nutrient rich filament and into clear warm water offshore. This is consonant with the observation / inference that albacore distributions are limited to clear offshore water because of the necessity of visually tracking their prey (Murphy, 1959). Similar factors also may affect the distribution of open ocean pelagic fish because even in the open ocean, frontal structures (e.g., Subtropical Front) play a major role in fish aggregation (Laurs and Lynn, 1977; Lynn, 1984).

The northern anchovy is another example of a fishery that is heavily constrained by upwelling processes. Off central California and in the Southern California Bight, spawning anchovies avoid cold upwelling waters (Lasker and Laurs, 1981). Their distribution of anchovy eggs obtained from *in situ* sampling superimposed on SST maps reveals an abrupt decline in the number of

eggs found near cold thermal fronts. Much of the cooler water found offshore of the Bight in their study appears to have originated north of Point Conception and near the coast of central California. The thermal preference of spawning anchovies for warm waters may reflect selection against those anchovy that spawn in cold filaments and thus have their eggs transported far offshore.

The examples cited above suggest that the accurate edge maps generated in this study could enhance fisheries management in these regions by providing a basis for modeling the spatial distribution of various species. For example, direct measures of habitat suitability in the basin model, as discussed by McCall (1990) remain elusive. Accurate satellite determination of oceanic fronts may allow the identification of dynamic habitat limits that change as a function of season and geographical location. In addition, if the filament generation processes are linked to upwelling processes, then the occurrence of such boundaries is likely to be strongly affected by large scale atmospheric forcing events like El Niño. Optimal management strategies depend on information about the mechanisms by which harvested individuals are replaced within the population (McCall, 1990). Accurate remote sensing data of the surface can aid in identifying the dominant replacement mechanisms (e.g., onshore vs. offshore transport, Parrish et al., 1981; Simpson, 1987). Moreover, the results of this study indicate that a quantitative parameterization of both the gradient angle and gradient magnitude of oceanic fronts, related by Euclidean distance to catch location and abundance, may prove to be an effective technique in the development of improved fisheries distribution models.

Other Uses of the Gradient Compression Technique

In this study, the angular compression of gradient information was used to look at long-term similarities and differences among different oceanic regions along the west coast of North America. This technique could also be used to differentiate between similar systems in other eastern boundary currents and to make comparisons between such systems. For example, it is hypothesized that, for filaments in eastern boundary currents in the southern hemisphere (e.g., Peru, Bengula Currents), a mirror image would be observed for the d-type / s-type filament boundary structure reported herein; that is, the most intense edges should occur between warm water to the north (i.e., nearest the equator) and cold water to the south. The gradient distributions could also be used to examine seasonal variability in filament characteristics if a sufficiently large, properly sampled (in time) image data set were available.

The compression analysis could be applied at a finer scale to investigate the transition zone in a given region and also the changing orientation of fronts across the shelf. Images like the ones in this study could be partitioned using a series of masks and then processed in the same way. This could specifically be used to look at the seasonal recurrence of filaments in relation to bathymetry and to sites of persistent upwelling. Such a study, however, would most likely benefit from the use of higher spatial resolution satellite data (e.g., Landsat TM, SPOT).

Limitations of This Study

The images chosen for each study region are widely distributed over a period of 10 years in order to maximize the statistical independence of each realization. Whole years are not represented in each region because suitable cloud-free images were not available. Thus, the data clearly are not appropriate for making seasonal inferences. Moreover, the images were compiled from months where past mean wind conditions were favorable for upwelling and thus do not reflect the general conditions in the California Current System during winter. Likewise, the data are not representative of meteorological conditions associated with large amounts of cloud cover. The database is adequate, however, to examine the long term characteristics of the thermal fronts in the CCS during months of known filament occurrence, and this is how it was used in this study. Also, the data set appears to be one of the more extensive compilations of AVHRR data off the west coast of North America yet to appear in the literature.

CONCLUSIONS

In this study, advanced cloud and land masking algorithms were used to construct uncontaminated maps of SST. Analysis of these uncontaminated maps shows that in the California Current System during months with upwelling winds, the weakest surface thermal fronts generally are oriented with warm water to the north / northwest and cold water to the south / southeast (120–160° according to the conventions in Fig. 4). Distributions of thermal gradient magnitude vs. gradient angle for the imagery of northern and Baja California appear similar in nature and are consistent with a sharp / diffuse boundary structure found in shipboard observations of filaments. Distributions of Region B suggest significant differences in thermal frontal structure compared to that of Regions A and C. This, and results from principal component analyses of the satellite imagery, show that two patterns of thermal gradient account for most of the temperature gradient variance in all three regions. The relative contribution of a given pattern, however, to the total thermal gradient variance varies from region to region.

This work was sponsored by the Marine Life Research Group (MLRG) of the Scripps Institution of Oceanography, and by grants from ONR and NASA. One of us (J. T. R.) received partial support in the form of a John D. Isaacs Marine Scholar-

ship sponsored by the California Sea Grant Program, National Oceanic and Atmospheric Administration. Satellite data were provided by the Scripps Satellite Oceanography Center. All image analysis was done in J. J. S.'s Image Analysis Laboratory. Data for Figure 2 (upwelling indices) were generously provided by A. Bakun.

One of us (J. T. R.) worked as a part-time undergraduate student during four summers in J. J. S.'s lab. I would like to thank J. J. S. for introducing me to remote sensing and digital image analysis techniques; I have truly learned the meaning of an iterative procedure. Darren Atkinson, Lance Al-Rawi, John Toman, and Tim Gallaudet assisted with the computer programming. Philip Misiowiec assisted with manuscript preparation. Guy Tapper and Nancy Hulbirt assisted with figure preparation. The SIO photo lab carefully produced the glossy prints from the gray scale originals.

This work also was supported in part by the National Sea Grant College Program, National Oceanic and Atmospheric Administration, U.S. Department of Commerce under grant number NA89AA-D-SG-138 and project numbers R/OE-25 and R/OE-27, and in part by the California State Resources Agency. The views expressed herein are those of the authors and do not necessarily reflect the views of NOAA or any of its subagencies. The U.S. government is authorized to reproduce and distribute this article for governmental purposes.

REFERENCES

Bakun, A. (1973), Coastal upwelling indices, west coast of North America, *NOAA Technical Report NMFS SSRF-671.*

Burdic, W.S. (1984), *Underwater Acoustic System Analysis,* Prentice-Hall, Englewood Cliffs, NJ.

Cattanach, D. (1970), A 16-channel digital acoustic telemetry system, in *IERE Conference Electronic Engineering in Ocean Technology.*

Cheesebrough, G. L., and Pittenger, R. F. (1991), Oceanography and the United States Navy, *Oceanus* 33:5–8.

Davis, R. E. (1985a), Drifter observations of coastal surface currents during CODE: the method and descriptive view, *J. Geophys. Res.* 90:4741–4755.

Davis, R. E. (1985b), Drifter observations of coastal surface currents during CODE: the statistical and dynamical view, *J. Geophys. Res.* 90:4756–4772.

Dewey, R. K., Moum, J. N., Paulson, C. A., Caldwell, D. R., and Pierce, S. D. (1991), Structure and dynamics of a coastal filament, *J. Geophys. Res.* 96:14,885–14,907.

Fasham, M. J. R. (1976), Misalignment angle and calibration of a two component electromagnetic log, *J. Navigation* 29: 76–81.

Flament, P., Armi, L., and Washburn, L. (1985), The evolving structure of an upwelling filament, *J. Geophys. Res.* 90: 11,765–11,778.

Gallaudet, T. C., and Simpson, J. J. (1991), Cloud screening of AVHRR imagery using split-and-merge clustering, *Remote Sens. Environ.* 38:77–121.

Gallaudet, T. C., and Simpson, J. J. (1994), Empirical orthogonal function analysis: applications to satellite-derived image data and the sea surface temperature variability off Punta Eugenia, *Remote Sens. Environ.*, forthcoming.

Hargreaves, P. M. (1975), Some observations on the relative abundance of biological sound scatters in the northeastern Atlantic Ocean, with particular reference to apparent fish shoals, *Mar. Biol. (Berl.)* 29:71–87.

Haury, L. R. (1984), An offshore eddy in the California Current system, IV, Plankton distributions, *Prog. Oceanogr.* 13:95–111.

Hayward, T. L., and Mantyla, A. M. (1990), Physical, chemical and biological structure of a coastal eddy near Cape Mendocino, *J. Mar. Res.* 48:825–850.

Hickey, B. H. (1979), The California Current System—hypotheses and fact, *Prog. Oceanogr.* 8:191–279.

Hotelling, H. (1933), Analysis of a complex statistical variables into principal components, *J. Ed. Psych.* 24:417–441; 498–520.

Huyer, A., and Kosro, P. M. (1987), Mesoscale surveys over the shelf and slope in the upwelling region near Pt. Arena, *J. Geophys. Res.* 92(C2):1655–1681.

Ingerbritsen, S.E., and Lyon, J. P. (1985), Principal component analysis of multitemporal image pairs, *Int. J. Remote Sens.* 6:687–696.

Jain, A. K. (1989), *Fundamentals of Digital Image Processing,* Prentice-Hall, Englewood Cliffs, NJ, 569 pp.

Jendro, L. M., Bourke, R. H., and Ramp, S. R. (1991), A range-dependent analysis of acoustic transmission across a cold filament in the California Current, in *Ocean Variability and Acoustic Propagation* (J. Potter and A. Warn-Varnasleds, Eds.) Kluwer Academic Publishers, Amsterdam, pp. 343–358.

Kelly, K. A. (1983), *Swirls and Plumes or the Application of Statistical Methods to Satellite Derived Surface Temperature,* Ref. 83-15, Scripps Institution of Oceanography, La Jolla, CA, 210 pp.

Kosro, P. M. (1987), Structure of the Coastal Current field off Northern California during the Coastal Ocean Dynamics Experiment, *J. Geophys. Res.* 92(C2):1637–1654.

Kosro, P. M., and Huyer, J. A. (1986), CTD and velocity surveys of seaward jets off northern California, July 1981 and 1982, *J. Geophys. Res.* 91:7680–7690.

Lasker, R. J., and Smith, P. M. (1978), Position of larval fish in an ecosystem, Rapports et Procés-verbaux de Réunions, Conseil International pour l'Exploration de la Mer, 173, pp. 77–84.

Lasker, R., Pelaez, J., and Laurs, R. M. (1981), The use of satellite infrared imagery for describing ocean processes in relation to the spawning of the northern anchovy (*Engraulis mordax*), *Remote Sens. Environ.* 11:439–453.

Lauritson, L., Nelson, G. G., and Porto, R. W. (1979), Data extraction and calibration of TIROS-N / NOAA A-G radiometers, NOAA Tech. Memo NESS 107, U.S. Department of Commerce, Washington, DC.

Laurs, R. M., and Lynn, R. J. (1977), Seasonal migration of North Pacific Albacore, *Thunnus alalunga,* into North American coastal waters: distribution, relative abundance, and association with transition zone waters, *Fisheries Bull.* 75: 795–822.

Laurs, R. M., Yuen, H. S. H., and Johnson, J. H. (1977), Small scale movements of albacore, *Thunnus alalunga,* in relation to ocean features as indicated by ultrasonic tracking and oceanographic sampling, *Fisheries Bull.* 75:347–355.

Laurs, R. M., Fiedler, P. C., and Montgomery, D. R. (1984), Albacore tuna catch distributions relative to environmental features observed from satellites, *Deep Sea Res.* 31:1085–1099.

Legeckis, R., and Pritchard, J. (1976). Algorithm for correcting VHRR imagery for geometric distortion due to earth curvature, earth rotation, and spacecraft roll attitude, NOAA

Tech. Memo NESS 77, U.S. Department of Commerce, Washington, DC.

Lynn, R. (1984), Measuring physical-oceanographic features relevant to the migration of fish, in *Mechanics of Migration of Fishes* (J. D. McCleave, G. P. Arnold, J. J. Dobson, and W. H. Neill, Eds.), pp 471–486.

Lynn, R. J., and Simpson, J. J. (1987), The California Current System: the seasonal variability of its physical characteristics, *J. Geophys. Res.* 92:12,947–12,996.

Lynn, R. J., Bliss, K. A., and Eber, L. E. (1982), Vertical and horizontal distributions of seasonal mean temperature, salinity, sigma-t, stability, dynamic height, oxygen and oxygen saturation in the California Current, 1950–1978, in *CalCOFI Atlas 30*, State of California Mar. Res. Comm., La Jolla, CA, 513 pp.

McCall, A. D. (1990), *Dynamic Geography of Marine Fish Populations*, Books in Recruitment Fisheries Oceanography, University of Washington Press, Seattle, WA.

Mellberg, L. E., Johannessen, O. M., Connors, D. N., Botseas, G., and Browning, D. G. (1987), Modeled acoustic propagation through an ice edge eddy in the East Greenland Sea marginal ice zone, *J. Geophys. Res.* 92:6857–6868.

Mellberg, L. E., Johannessen, O. M., Connors, D. N., Botseas, G., and Browning, D. G. (1991), Acoustic propagation in the western Greenland Sea frontal zone, *J. Acoust. Soc. Am.* 89:2137–2156.

Mercer, J. A., and Booker, J. R. (1983), Long range propagation of sound through oceanic mesoscale structures, *J. Geophys. Res.* 88:689–699.

Mitson, R. B. (1983), Fisheries sonar (incorporating underwater observation using SONAR by D. G. Tucker), in *The Detection of Fish* (David Cushing, Ed.), Pergamon, Oxford.

Mooers, C. N. K., and Robinson, A. R. (1984), Turbulent jets and eddies in the California Current and inferred cross-shore transport, *Science* 223:51–53.

Murphy, G. I. (1959), Effects of water purity on albacore catches, *Limnol. Oceanogr.* 4:86–93.

Okamato, M. (1969), Optimality of principal components, in *Multivariate Analysis—II* (P. R. Krishnaiak, Ed.), Academic, New York.

Owen, R. W. (1989), Microscale and finescale variations of small plankton in coastal and pelagic environments. *J. Mar. Res.* 47:197–240.

Parrish, P. H., Nelson, C., and Bakun, A. (1981), Transport mechanisms and the reproductive success of fishes in the California Current, *Biol. Oceanogr.* 1:175–202.

Preisendorfer, R. W. (1988), *Principal Component Analysis in Meteorology and Oceanography*, Elsevier, Amsterdam.

Ramp, S. R., Jessen, P. F., Brink, K. H., Niiler, P. P., Daggett, F. L., and Best, J. S. (1991), The physical structure of filaments near Point Arena, California during June, 1987, *J. Geophys. Res.* 96:14,859–14,883.

Regier, L. (1982), Mesoscale current fields observed with a shipboard acoustic current meter, *J. Phys. Oceanogr.* 12: 880–886.

Richards, J. A. (1986), *Remote Sensing Digital Image Analysis: An Introduction*, Springer-Verlag, New York.

Richman, M. B. (1986), Rotation of principal components, *J. Climatol.* 6:293–335.

Rienecker, M. M., and Mooers, C. N. K. (1989). Mesoscale eddies, jets, and fronts off Point Arena, California, July 1986, *J. Geophys. Res.* 94:12,555–12,570.

Rienecker, M. M., Mooers, C. N. K., Hagan, D. E., and Robinson, A. R. (1985), A cool anomaly off Northern California: an investigation using IR imagery and in situ data, *J. Geophys. Res.* 90:4807–4818.

Roberts, W. J. M. (1971), Charting a telephone cable, *Hydrospace* 4:47–50.

Robinson, M. K. (1976), Atlas of North Pacific monthly mean temperatures and mean salinities of the surface layer, Naval Oceanographic Office Reference Publication No. 2, Department of the Navy, Washington, DC.

Rousseau, T. H., Siegmann, W. L., and Jacobson, M. J. (1982), Acoustic propagation through a model of shallow fronts in the deep ocean, *J. Acoust. Soc. Am.* 72:924–936.

Simpson, J. J. (1984), An offshore eddy in the California Current system, III, Chemical structure, *Prog. Oceanogr.* 13:71–93.

Simpson, J. J. (1985), Air-sea exchange of carbon dioxide and oxygen induced by phytoplankton: Methods and interpretation, in *Mapping Strategies in Chemical Oceanography* (A. Zirino, Ed.), American Chemical Society, Washington, DC, pp. 409–450.

Simpson, J. J. (1987), Transport processes affecting the survival of pelagic fish stocks in the California Current, *Am. Fisheries Soc. Symp.* 2:39–60.

Simpson, J. J. (1990), On the accurate detection and enhancement of oceanic features observed in satellite data, *Remote Sens. Environ.* 33:17–33.

Simpson, J. J. (1992), Image masking using polygon fill and morphological operations, *Remote Sens. Environ.* 40:161–183.

Simpson, J. J., and Humphrey, C. (1990), An automated cloud screening algorithm for daytime Advanced Very High Resolution Radiometer imagery, *J. Geophys. Res.* 95:13,459–13,481.

Simpson, J. J., and Lynn, R. J. (1990), A mesoscale eddy dipole in the offshore California Current, *J. Geophys. Res.* 95: 13,009–13,022.

Simpson, J. J., Dickey, T. D., and Koblinsky, C. J. (1984), An offshore eddy in the California Current system, Part I: Interior dynamics, *Prog. Oceanogr.* 13:15–49.

Strub, P. T., Kosro, P. M., and Huyer, A. (1991), The nature of the cold filaments in the California Current system, *J. Geophys. Res.* 96:14,743–14,768.

Thomas, A. C., and Emery, W. J. (1988), Relationships between near-surface plankton concentrations, hydrography, and satellite-measured sea surface temperature, *J. Geophys. Res.* 93:15,733–15,748.

Traganza, E. D., Conrad, J. C., and Brealeer, L. C. (1981), Satellite observations of a s-type upwelling system and giant plume in the California Current, in *Coastal Upwelling* (F. A. Richards, Ed.), American Geophysical Union, Washington, DC, pp. 228–241.

Uscinski, B. J., Potter, J. R., and Akal, T. (1989), Broadband acoustic transmission fluctuations during NAPOLI 85, an experiment in the Tyrrhenian Sea: preliminary results and arrival time analysis, *J. Acoust. Soc. Am.* 86:706–715.

Wahl, D. D., and Simpson, J. J. (1990), Physical processes affecting the objective determination of near-surface velocity from satellite data, *J. Geophys. Res.* 95:13,511–13,528.

Washburn, L., and Armi, L. (1988), Observations of frontal instabilities on an upwelling filament, *J. Phys. Oceanogr.* 18:1075–1092.